Magnetic charges and magnetoelectricity in hexagonal rare-earth manganites and ferrites

Meng Ye[*] and David Vanderbilt

Department of Physics & Astronomy, Rutgers University, Piscataway, New Jersey 08854, USA

Magnetoelectric (ME) materials are of fundamental interest and show broad potential for technological applications. The common dominant contribution to the ME response is the lattice-mediated one, which is proportional to both the Born electric charge Z^e and its analog, the dynamical magnetic charge Z^m. Our previous study has shown that exchange striction acting on noncollinear spins induces much larger magnetic charges than those that depend on spin-orbit coupling. The hexagonal manganites $R\mathrm{MnO}_3$ and ferrites $R\mathrm{FeO}_3$ ($R =$ Sc, Y, In, Ho-Lu) exhibit strong couplings between electric, magnetic, and structural degrees of freedom. The transition-metal ions in the basal plane antiferromagnetically coupled through super-exchange so as to form a $120°$ noncollinear spin arrangement. In this paper, we present a theoretical study of the magnetic charges, and of the spin-lattice and spin-electronic ME constants, in these hexagonal manganites and ferrites. We clarify the conditions under which exchange striction leads to enhanced Z^m values and anomalously large in-plane spin-lattice ME effects.

I. INTRODUCTION

The cross coupling between magnetic, electric, and elastic properties can lead to a plethora of novel and profound physical phenomena, with potentially broad and innovative applications. Magnetoelectric (ME) effects are those in which the electric polarization **P** responds to an applied magnetic field **H** or magnetization **M** responds to an applied electric field $\mathcal{E}$. The ME coupling (MEC) between magnetic and electric properties has motivated intense experimental and theoretical investigations in bulk single crystals, thin films, composite layers, and organic-inorganic hybrid materials in recent years [1–11].

At the linear-response level, the linear MEC tensor α is defined as

$$\alpha_{\beta\nu} = \left.\frac{\partial P_\beta}{\partial H_\nu}\right|_{\mathcal{E}} = \mu_0 \left.\frac{\partial M_\nu}{\partial \mathcal{E}_\beta}\right|_{\mathbf{H}}, \tag{1}$$

where indices β and ν denote the Cartesian directions and μ_0 is the vacuum permeability. From a theoretical point of view, the linear ME effect can be decomposed into electronic (frozen-ion), ionic (lattice-mediated), and strain-mediated responses [11]. Each term can be further subdivided into spin and orbital contributions based on the origin of the induced magnetization. As the orbital moment is usually strongly quenched on the transition-metal sites, most phenomenological and first-principles studies have focused on the spin-electronic [12] and the spin-lattice [13–15] contributions. The lattice response can be written, following Ref. [13], as

$$\alpha_{\beta\nu}^{\mathrm{latt}} = \Omega_0^{-1} \mu_0 Z_{m\beta}^e (K^{-1})_{mn} Z_{n\nu}^m \tag{2}$$

(sum over repeated indices implied), i.e., as a matrix product of the dynamical Born electric charge Z^e, the inverse force-constant matrix K^{-1}, and the dynamical magnetic charge Z^m, where m and n are composite labels for an atom and its displacement direction. Ω_0 is the unit cell volume. Note that

---

*mengye@physics.rutgers.edu

Z^m is the magnetic analog of the dynamical Born charge, and is defined as

$$Z_{m\nu}^m = \Omega_0 \left.\frac{\partial M_\nu}{\partial u_m}\right|_{\mathcal{E},\mathbf{H},\eta} = \mu_0^{-1} \left.\frac{\partial F_m}{\partial H_\nu}\right|_{\mathcal{E},\mathbf{u},\eta}, \tag{3}$$

where u_m is an internal displacement, F_m is an atomic force, and η is a homogeneous strain. In principle, Z^m has both spin and orbital parts, corresponding, respectively, to spin and orbital contributions to M_ν. This is also equivalent to Zeeman and $\mathbf{p} \cdot \mathbf{A}$ terms induced by H_ν. However, in this paper, we shall focus on the spin part in the following. Our previous first-principles study has shown that exchange striction acting on noncollinear spin structures induces much larger magnetic charges than when Z^m is driven only by spin-orbit coupling (SOC). Therefore, exchange striction provides a promising mechanism for obtaining large MECs [16].

The hexagonal manganites $R\mathrm{MnO}_3$ and ferrites $R\mathrm{FeO}_3$ ($R =$ Sc, Y, In, and Ho-Lu) form an interesting class of materials exhibiting strong couplings between electric, magnetic, and structural degrees of freedom [17]. A series of first-principles [15,18–20] and phenomenological [21] studies have greatly enhanced our understanding of the coupled properties. The ferroelectricity is induced by the structural trimerization, and the direction of the spontaneous polarization is related to the trimerization pattern [19]. An interesting "cloverleaf" pattern formed from interlocking domain walls between structural and ferroelectric domains has been found in hexagonal $R\mathrm{MnO}_3$ and is now understood in terms of Landau theory [21–23]. Hexagonal $R\mathrm{MnO}_3$ and $R\mathrm{FeO}_3$ have rich magnetic phase diagrams and show considerable potential for manipulation and practical applications [24–26]. The magnetic order has two different origins, with the transition-metal Mn^{3+} or Fe^{3+} sublattices ordering first, often followed by ordering of the rare-earth ions R^{3+} at lower temperature. The magnetic anisotropy is easy-plane and easy-axis for $3d$ and $4f$ spins, respectively; the $3d$ moments are antiferromagnetically coupled through superexchange so as to form a $120°$ noncollinear arrangement in the x-y plane, while the $4f$ rare-earth moments are collinear along the hexagonal z axis.

The low-temperature magnetic phases of RMnO$_3$ and RFeO$_3$ allow a linear ME effect to be present. The recently developed ME force microscopy technique has been used successfully to observe the ME domains in ErMnO$_3$ [27]. In that paper, a large ME component $\alpha_{zz} \sim 13$ ps/m has been measured at 4 K, which is below the Mn^{3+} ordering temperature of 81 K but above the Er^{3+} ordering temperature of 2 K. Recently, a first-principles study has been conducted for this SOC-induced ME response in ErMnO$_3$, but the spin-lattice α_{zz} arising from the Mn^{3+} order was found to be only 0.7–1.0 ps/m. This discrepancy suggests that the dominant ME effect in the hexagonal $\hat{z}$ direction is mediated by the Er^{3+} $4f$ electrons in ErMnO$_3$. The in-plane ME effect, which has not been measured or calculated, has a different origin. It is dominated by an exchange-striction mechanism on the Mn^{3+} sublattice, because the noncollinear spin pattern is sensitive to the lattice distortion. Thus, hexagonal RMnO$_3$ and RFeO$_3$ are good candidates to show exchange-striction enhanced magnetic charges and anomalously large spin-lattice MECs.

In this paper, we use first-principles density-functional methods to study the magnetic charges and the spin-induced MECs arising from the $3d$ electrons in hexagonal HoMnO$_3$, ErMnO$_3$, YbMnO$_3$, LuMnO$_3$, and LuFeO$_3$. For the transverse magnetic charge components and MECs, we also provide a comparison between results induced solely by exchange striction and ones including SOC. Our results confirm that the exchange striction greatly enhances the in-plane magnetic charges, while the SOC contribution is minor for most components except on Mn atoms. However, the effect of SOC on the MECs is surprisingly large in many cases. This occurs because the exchange-striction contribution tends to be reduced by cancellations between modes, while the SOC contribution is mainly amplified by a few low-frequency modes. The in-plane ME responses are discussed case by case and the conditions under which exchange striction leads to anomalously large in-plane spin-lattice MECs are clarified.

The paper is organized as follows. In Sec. II A and II B we introduce the geometric structure and magnetic order of hexagonal RMnO$_3$ and RFeO$_3$. In Sec. II C we analyze the tensor symmetries of the Born charges, magnetic charges, and MECs in two different magnetic phases of RMnO$_3$ and RFeO$_3$. The computational details are described in Sec. II D. The results and discussion of Born charges, magnetic charges, and MECs in RMnO$_3$ and LuFeO$_3$ are presented in Sec. III. We summarize and give our conclusions in Sec. IV.

II. PRELIMINARIES

A. Hexagonal RMnO$_3$

Above the structural transition temperature $T_c \sim 900 - 1500$ K, the hexagonal manganites RMnO$_3$ ($R =$ Sc, Y, In, and Ho-Lu) are paraelectric insulators. The space group is P6$_3$/mmc with two formula units (f.u.) per primitive cell. Below T_c, the size mismatch between the small-radius R^{3+} ion and the large MnO$_5$ bipyramid leads to an inward tilting of the three corner-shared MnO$_5$ polyhedra and an associated "one-up/two-down" buckling of the R^{3+} ion layer,
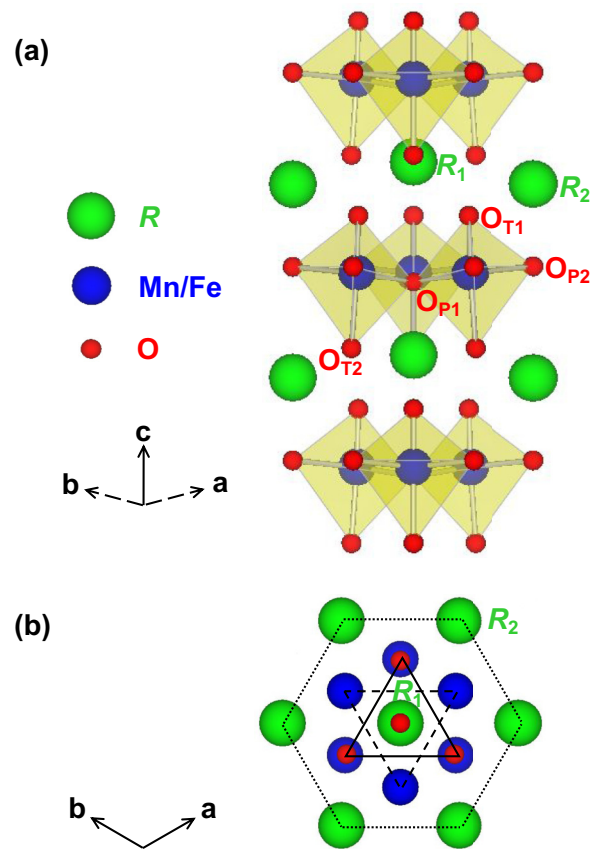

FIG. 1. (Color online) Structure of ferroelectric hexagonal RMnO$_3$ (6 f.u. per primitive cell). (a) Side view from [110]. (b) Plan view from [001]; dashed (solid) triangle indicates three Mn^{3+} connected via O$_{P1}$ to form a triangular sublattice at $z = 0$ ($z = 1/2$).

as shown in Fig. 1. The transition triples ("trimerizes") the unit cell, lowers the structural symmetry to P6$_3$cm, and induces ferroelectricity. As the induced polarization is nonlinearly coupled to the trimerization, these systems are improper ferroelectrics [18,19,21].

The Mn^{3+} magnetic order develops below the Néel temperature T_N of $\sim 70 - 130$ K. The in-plane Mn-O-Mn superexchange determines the noncollinear 120° antiferromagnetic (AFM) order on the Mn^{3+} triangular lattice. On the other hand, the inter-plane Mn-O-R-O-Mn exchange, which is two orders of magnitude weaker than the in-plane exchange, modulates the relative spin directions between two consecutive Mn planes [15,24]. At temperatures lower than ~ 5.5 K, the rare-earth ions with partially filled $4f$ shells develop collinear spin order along the hexagonal z direction. For the Mn^{3+} order, there are four distinct magnetic phases, namely A$_1$ (P6$_3$cm), A$_2$ (P6$_3$c$'$m$'$), B$_1$ (P6$_3'$cm$'$), and B$_2$ (P6$_3'$c$'$m). The linear ME effect exists only in A$_1$ and A$_2$ phases. The A$_1$ and A$_2$ phases are shown in Fig. 2; the B$_1$ and B$_2$ phases can be obtained from A$_2$ and A$_1$ by reversing the spins on the dashed triangles. From previous experiments, it is known that at zero temperature without a magnetic field, HoMnO$_3$ is in the A$_1$ phase, while ErMnO$_3$, YbMnO$_3$, and LuMnO$_3$ are not in either A phase. Under a weak magnetic field along the $\hat{z}$ direction, ErMnO$_3$ and YbMnO$_3$ undergo a transition into the A$_2$ phase [24–26].
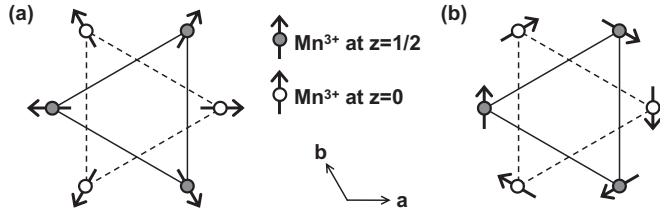
FIG. 2. Magnetic phases of hexagonal RMnO$_3$ and RFeO$_3$. Mn^{3+} ions form triangular sublattices at $z = 0$ (dash line) and $z = 1/2$ (solid line). (a) A$_2$ phase with magnetic symmetry P6$_3$c$'$m$'$; spins on a given Mn^{3+} layer point all in or all out. (b) A$_1$ phase with the magnetic symmetry P6$_3$cm, with Mn^{3+} spins pointing tangentially to form a vortex pattern. The A$_1$ and A$_2$ phases differ by a 90° global rotation of the spins. The B$_1$ and B$_2$ phases can be obtained from A$_2$ and A$_1$ by reversing the spins on the dashed triangles.

B. Hexagonal RFeO$_3$

Epitaxially grown thin-film hexagonal RFeO$_3$ has a similar structure as hexagonal RMnO$_3$, with improper ferroelectricity below ~1000 K. Replacing Mn^{3+} with Fe^{3+} introduces larger spin moments and stronger super-exchange interactions in the basal plane. In a recent experiment, AFM order has been found to develop at $T_N = 440$ K followed by a spin-reorientation transition below $T_R = 130$ K in LuFeO$_3$ [28]. It has also been confirmed that below 5 K, the magnetic structure of LuFeO$_3$ is that of the A$_2$ phase [29].

C. Symmetry

Our purpose is to understand the mechanisms that generate large magnetic charges that may in turn induce anomalously large spin-lattice MECs. Therefore, we focus on the A$_1$ and A$_2$ magnetic phases, shown in Fig. 2, which allow a linear MEC to exist. ErMnO$_3$, YbMnO$_3$, and LuMnO$_3$ actually adopt other phases as their ground-state magnetic order at low temperature. Nevertheless, we include them for purposes of comparison when calculating the properties of the hexagonal RMnO$_3$ materials in the A$_2$ phase. We also study LuFeO$_3$ in the A$_2$ phase, and for HoMnO$_3$ we study both the A$_1$ and A$_2$ phases.

The A$_1$ and A$_2$ phases have the same P6$_3$cm structural symmetry, so the forms of the atomic Born charge tensors in the two phases are the same. The Born charges for R_1 and O$_{P1}$ take the tensor form shown in Table I(a), while those of R_2 and O$_{P2}$ have the symmetry pattern shown in Table I(b). For the Mn, Fe, O$_{T1}$, and O$_{T2}$ sites lying on a vertical M_y mirror plane, the Born charges are as given in Table I(c); for the partner sites related by rotational symmetry, the tensors also need to be rotated accordingly.

The symmetry forms of the atomic magnetic charge tensors can be derived from the on-site magnetic point symmetries. For the A$_1$ phase, the magnetic space group is P6$_3$cm and the magnetic charges of R_1 and O$_{P1}$ take the forms given in Table I(d), those for R_2 and O$_{P2}$ have the tensor symmetry shown in Table I(b), and for Mn, Fe, O$_{T1}$, and O$_{T2}$ they can be written in the form of Table I(e). For the A$_2$ phase, the magnetic group is P6$_3$c$'$m$'$; all the improper operators are associated with the time-reversal operation, so the magnetic charges have the same tensor forms as the Born charges.

TABLE I. Symmetry patterns of Born charges Z^e, magnetic charges Z^m, and ME tensors α in RMnO$_3$ and RFeO$_3$. Patterns for Mn, Fe, O$_{T1}$, and O$_{T2}$ are for atoms lying on an M_y mirror plane. Unless otherwise specified, patterns apply to both A$_1$ and A$_2$ phases.

(a)	$\begin{pmatrix} \bullet & & \\ & \bullet & \diagdown \\ & & \bullet \end{pmatrix}$	α (A$_2$ only) Z^e on R_1 and O$_{P1}$ Z^m on R_1 and O$_{P1}$ (A$_2$ only)
(b)	$\begin{pmatrix} & \times & \\ \times & & \\ & & \bullet \end{pmatrix}$	Z^e on R_2 and O$_{P2}$ Z^m on R_2 and O$_{P2}$
(c)	$\begin{pmatrix} \bullet & & \bullet \\ & \bullet & \\ \bullet & & \bullet \end{pmatrix}$	Z^e on Mn, Fe, O$_{T1}$, and O$_{T2}$
(d)	$\begin{pmatrix} & & \\ & \diagup & \\ \circ & & \end{pmatrix}$	α (A$_1$ only) Z^m on R_1 and O$_{P1}$ (A$_1$ only)
(e)	$\begin{pmatrix} & \bullet & \\ \bullet & & \bullet \\ & \bullet & \end{pmatrix}$	Z^m on Mn, Fe, O$_{T1}$, and O$_{T2}$ (A$_1$ only)

$\bullet\!\!-\!\!\bullet$ equal component.
$\bullet\!\!-\!\!\circ$ equal magnitude with opposite sign.

A symmetry analysis of the structure and the magnetic space group identifies the phonon modes that couple to the electromagnetic field. The infrared (IR)-active phonon modes that couple to the electric field are the longitudinal A_1 modes and the transverse E_1 modes,

$$\Gamma_{IR} = 10A_1 + 15E_1, \tag{4}$$

including the three acoustic modes. The magnetization is generated by phonon modes that couple to the magnetic field. In the A$_1$ phase, the magneto-active phonon modes are the longitudinal A_2 modes and the transverse E_1 modes,

$$\Gamma_{mag}^{A_1} = 5A_2 + 15E_1, \tag{5}$$

where one pair of acoustic E_1 modes are included. In the A$_2$ phase, on the other hand, the IR- and magneto-active phonon modes are identical, since the magnetic and Born charge tensors have the same form in this case.

For the MECs in the A$_1$ phase, as the longitudinal IR-active and magneto-active modes are mutually exclusive, the ME tensor takes the form of Table I(d), which does not have a longitudinal ME component. For the A$_2$ magnetic phase, the A_1 and E_1 modes are both IR-active and magneto-active, so that the ME tensor has both longitudinal and transverse components and adopts the form shown in Table I(a).

D. First-principles methods

Our calculations are performed with plane-wave density functional theory (DFT) implemented in VASP [30] using the generalized-gradient approximation parametrized by the Perdew-Burke-Ernzerhof functional [31]. The ionic core environment is simulated by projector augmented wave (PAW) pseudopotentials [32], and the $4f$ electrons are placed in the PAW core. We use a Hubbard $U = 4.5$ eV and $J = 0.95$ eV on the d orbitals of the Mn/Fe atoms, and the moments on the rare-earth ions are not considered [15]. The structures are fully relaxed in the DFT+U [33] calculations

with their noncollinear spin arrangements in two cases: when SOC is present and when it is absent. In our noncollinear magnetization calculation, a high cutoff energy 700 eV and a tight energy error threshold 1.0×10^{-9} eV are necessary to get fully converged magnetic properties. The Born effective charge tensors and the Γ-point force-constant matrices are obtained using linear-response methods in the absence of SOC. The dynamical magnetic charges are computed by applying a uniform Zeeman field [12] to the crystal and computing the resulting forces. Polarization is calculated using the Berry phase formalism [34]. A $4 \times 4 \times 2$ Γ-centered k-point mesh is used in the calculations.

III. RESULTS AND DISCUSSION

A. Born charge and force-constant matrix

The f electrons are not included in our calculations for the hexagonal RMnO$_3$ class of materials, so the major differences between compounds result from the variation of the rare-earth radius; the trimerization tends to increase as the radius of the rare-earth element decreases. Because of the similarity in the geometric structures, the dielectric and phonon properties are almost identical in the RMnO$_3$ compounds, regardless of the magnetic ordering. In Tables II and III we list the Born charge tensors and the eigenvalues of the force-constant matrix for the IR-active modes of LuMnO$_3$ and LuFeO$_3$. Only small differences are observed between LuMnO$_3$ and LuFeO$_3$, reflecting the different transition-metal atom. The results for the other RMnO$_3$ compounds are quite similar to those of LuMnO$_3$ and are given for completeness in the Supplemental Material [35].

B. Magnetization and magnetic charge

In the A$_2$ phase, the trimerization induces not only an electric polarization, but also a weak ferromagnetism in the $\hat{z}$ direction resulting from a SOC-induced tilting of the Mn^{3+} spin moments. The net magnetizations in the 30-atom unit cell for A$_2$-phase HoMnO$_3$, ErMnO$_3$, YbMnO$_3$, and LuMnO$_3$ are 0.309, 0.303, 0.292, and 0.268 μ_B, respectively. These magnetic moments are found to depend almost linearly on

TABLE III. Eigenvalues of the force-constants matrix (eV/Å^2) for IR-active modes in LuMnO$_3$ and LuFeO$_3$ in the A$_2$ phase, excluding translational modes.

A_1 modes		E_1 modes	
LuMnO$_3$	LuFeO$_3$	LuMnO$_3$	LuFeO$_3$
4.24	3.48	3.32	3.56
7.44	6.70	4.68	4.62
8.74	8.41	6.73	6.97
11.51	11.47	7.35	8.09
14.01	12.03	8.63	8.83
15.60	15.59	9.56	9.24
22.66	20.53	11.36	11.37
25.87	22.83	12.46	12.46
35.82	28.46	13.02	13.85
		14.09	14.92
		16.49	16.87
		17.37	17.35
		23.36	21.19
		37.75	28.75

the tilting angle of the MnO$_5$ bipyramids, which takes values of 5.03°, 5.07°, 5.16°, and 5.21° respectively in these four compounds, but in any case the variation is not very large. In contrast, the result for LuFeO$_3$ is -0.077 μ_B, which is much smaller and of opposite sign compared with the RMnO$_3$ materials.

The magnetic charges defined in Eq. (3) are more sensitive to the local environment, and now the differences between RMnO$_3$ compounds are more significant. We divide the magnetic charge components into two groups that we label as "longitudinal" and "transverse" depending on whether the coupling is to magnetic fields along the $\hat{z}$ direction or in the x-y plane, respectively.[1]

The longitudinal magnetic charge components are calculated with a magnetic field directed along $\hat{z}$, which is roughly

---

[1]Note that this differs from the usual convention for the magnetic susceptibility, where the distinction between "longitudinal" and "transverse" corresponds to the direction of the applied field relative to the spin direction.

TABLE II. Atomic Born charge tensors Z^{e} (in units of $|e|$) for LuMnO$_3$ and LuFeO$_3$ in the A$_2$ phase. TM = Mn or Fe.

	LuMnO$_3$	LuFeO$_3$		LuMnO$_3$	LuFeO$_3$
$Z^{\mathrm{e}}_{xx}(\mathrm{Lu_1})$	3.61	3.79	$Z^{\mathrm{e}}_{xz}(\mathrm{O_{T1}})$	0.19	0.11
$Z^{\mathrm{e}}_{zz}(\mathrm{Lu_1})$	4.12	3.94	$Z^{\mathrm{e}}_{zz}(\mathrm{O_{T1}})$	-3.19	-3.21
$Z^{\mathrm{e}}_{xx}(\mathrm{Lu_2})$	3.66	3.84	$Z^{\mathrm{e}}_{xx}(\mathrm{O_{T2}})$	-1.90	-2.15
$Z^{\mathrm{e}}_{yx}(\mathrm{Lu_2})$	0.13	0.15	$Z^{\mathrm{e}}_{zx}(\mathrm{O_{T2}})$	-0.20	-0.19
$Z^{\mathrm{e}}_{zz}(\mathrm{Lu_2})$	3.96	3.88	$Z^{\mathrm{e}}_{yy}(\mathrm{O_{T2}})$	-1.85	-2.13
$Z^{\mathrm{e}}_{xx}(\mathrm{TM})$	3.17	2.96	$Z^{\mathrm{e}}_{xz}(\mathrm{O_{T2}})$	-0.18	-0.11
$Z^{\mathrm{e}}_{zx}(\mathrm{TM})$	0.44	0.21	$Z^{\mathrm{e}}_{zz}(\mathrm{O_{T2}})$	-3.33	-3.30
$Z^{\mathrm{e}}_{yy}(\mathrm{TM})$	3.26	3.01	$Z^{\mathrm{e}}_{xx}(\mathrm{O_{P1}})$	-3.00	-2.40
$Z^{\mathrm{e}}_{xz}(\mathrm{TM})$	0.07	-0.02	$Z^{\mathrm{e}}_{zz}(\mathrm{O_{P1}})$	-1.54	-1.61
$Z^{\mathrm{e}}_{zz}(\mathrm{TM})$	3.95	4.16	$Z^{\mathrm{e}}_{xx}(\mathrm{O_{P2}})$	-3.05	-2.45
$Z^{\mathrm{e}}_{xx}(\mathrm{O_{T1}})$	-1.92	-2.19	$Z^{\mathrm{e}}_{yx}(\mathrm{O_{P2}})$	-0.03	-0.02
$Z^{\mathrm{e}}_{zx}(\mathrm{O_{T1}})$	0.25	0.25	$Z^{\mathrm{e}}_{zz}(\mathrm{O_{P2}})$	-1.43	-1.52
$Z^{\mathrm{e}}_{yy}(\mathrm{O_{T1}})$	-2.00	-2.28			

TABLE IV. Longitudinal magnetic charge components Z^{m} ($10^{-3}\mu_B$/Å) of RMnO$_3$ and LuFeO$_3$ in the A$_2$ phase. All components vanish in the absence of SOC.

	HoMnO$_3$	ErMnO$_3$	YbMnO$_3$	LuMnO$_3$	LuFeO$_3$
$Z^{\mathrm{m}}_{zz}(\mathrm{R_1})$	-50	-53	-53	-67	7
$Z^{\mathrm{m}}_{zz}(\mathrm{R_2})$	14	35	24	16	7
$Z^{\mathrm{m}}_{xz}(\mathrm{TM})$	-92	-86	-61	-67	9
$Z^{\mathrm{m}}_{zz}(\mathrm{TM})$	24	1	6	25	2
$Z^{\mathrm{m}}_{xz}(\mathrm{O_{T1}})$	-49	-44	-41	-19	23
$Z^{\mathrm{m}}_{zz}(\mathrm{O_{T1}})$	99	81	53	33	22
$Z^{\mathrm{m}}_{xz}(\mathrm{O_{T2}})$	-7	-12	-12	-12	0
$Z^{\mathrm{m}}_{zz}(\mathrm{O_{T2}})$	-119	-94	-64	-49	-25
$Z^{\mathrm{m}}_{zz}(\mathrm{O_{P1}})$	-276	-257	-230	-190	54
$Z^{\mathrm{m}}_{zz}(\mathrm{O_{P2}})$	141	140	125	100	-35

TABLE V. Transverse magnetic charge components Z^m ($10^{-2}\mu_B$/Å) of HoMnO$_3$ in the A$_1$ phase, as computed including or excluding SOC.

	Total	No SOC		Total	No SOC
Z^m_{yx}(Ho$_1$)	-25	-28	Z^m_{zy}(O$_{T1}$)	-188	-230
Z^m_{yx}(Ho$_2$)	-15	-18	Z^m_{yx}(O$_{T2}$)	-57	-67
Z^m_{xx}(Ho$_2$)	-1	3	Z^m_{yx}(O$_{T2}$)	-20	-26
Z^m_{yx}(Mn)	92	54	Z^m_{zy}(O$_{T2}$)	-192	-231
Z^m_{xy}(Mn)	-10	2	Z^m_{yx}(O$_{P1}$)	-483	-551
Z^m_{zy}(Mn)	41	48	Z^m_{xx}(O$_{P2}$)	395	461
Z^m_{yx}(O$_{T1}$)	23	28	Z^m_{yx}(O$_{P2}$)	184	253
Z^m_{xy}(O$_{T1}$)	-7	-7			

perpendicular to the spin directions. These components are only nonzero when SOC is considered. The scenario here is similar to the case of a transverse magnetic field (H_x or H_y) applied to Cr$_2$O$_3$, since the magnetization is along the z axis for Cr$_2$O$_3$. It is therefore not surprising to find that the longitudinal magnetic charges of RMnO$_3$ and LuFeO$_3$ in Table IV are comparable to the SOC-induced transverse magnetic charges in Cr$_2$O$_3$ [16]. The longitudinal magnetic charges for O$_{P1}$ and O$_{P2}$ in LuFeO$_3$ are opposite to, and about three times smaller than, the ones in RMnO$_3$. Considering the fact that the trimerization distortion involves vertical displacements of O$_{P1}$ and O$_{P2}$, these results explain the differences between RMnO$_3$ and LuFeO$_3$ regarding the magnitude and the direction of the weak ferromagnetism.

For the response to transverse magnetic fields, both the field and the spins lie in the basal plane, so the dynamical magnetic charges are driven by both SOC and exchange striction. As the exchange-striction strength can exceed that of the SOC by orders of magnitude in some materials, it is worthwhile to understand the relative size of these two effects in RMnO$_3$ and LuFeO$_3$. In Tables V and VI we present the transverse magnetic charges induced with and without SOC

in the A$_1$ and A$_2$ phases. It is obvious that the exchange-striction contributions are an order of magnitude larger for many transverse components. Similarly, the magnetic charges induced by exchange striction are about ten times stronger than the SOC-driven longitudinal ones in Table IV (notice the units in Table IV are different from Tables V and VI). The largest transverse magnetic charge contributions are from exchange striction on the O atoms, which mediate the superexchange between Mn atoms. For the Mn atoms themselves, on the other hand, the exchange-striction contribution is much weaker, and comparable in strength to the SOC-induced contributions. Since the signs of these two contributions are not correlated, a partial cancellation or even a sign reversal sometimes occurs, as can be seen by inspecting the results for the Mn atoms in Tables V and VI. The transverse magnetic charges on the Mn atoms are thus especially sensitive to SOC.

C. Magnetoelectric effect

We calculate the spin-lattice MEC from Eq. (2) using our computed Born charges, force-constant matrices, and magnetic charges. The spin-electronic contributions are calculated based on the $\partial P/\partial H$ version of Eq. (1) with the lattice degrees of freedom frozen. We further subdivide the ME tensor components into longitudinal and transverse ones based on the direction of **H** relative to the hexagonal axis as before, so that the longitudinal (transverse) spin-lattice MEC is calculated using the longitudinal (transverse) magnetic charge components. The MEC tensor elements allowed by symmetry are the longitudinal α_{zz} and transverse $\alpha_{xx} = \alpha_{yy}$ ones in the A$_2$ phase, and only the transverse $\alpha_{yx} = -\alpha_{xy}$ components in the A$_1$ phase.

In the first part of Table VII, the spin-contributed longitudinal MECs are shown for RMnO$_3$ and LuFeO$_3$ in the A$_2$ phase. The MEC from the spin channel is dominated by the spin-lattice contribution. Although the longitudinal magnetic charges of LuFeO$_3$ are smaller than for RMnO$_3$, the spin-lattice MECs $|\alpha_{zz}|$ in RMnO$_3$ and LuFeO$_3$ are similar,

TABLE VI. Transverse magnetic charge components Z^m ($10^{-2}\mu_B$/Å) of RMnO$_3$ and LuFeO$_3$ in the A$_2$ phase, as computed including or excluding SOC.

	HoMnO$_3$		ErMnO$_3$		YbMnO$_3$		LuMnO$_3$		LuFeO$_3$	
	Total	No SOC	Total	No SOC	Total	No SOC	Total	No SOC	Total	No SOC
Z^m_{xx}(R$_1$)	-23	-24	-21	-22	-37	-40	-42	-35	-36	-52
Z^m_{xx}(R$_2$)	6	-1	6	3	12	9	14	6	15	24
Z^m_{yx}(R$_2$)	16	18	11	12	10	10	8	7	-9	-11
Z^m_{xx}(TM)	-2	10	-7	-10	-16	-21	-11	1	-52	-43
Z^m_{zx}(TM)	-42	-24	-38	-22	-25	-34	-31	-17	-102	-95
Z^m_{yy}(TM)	-5	46	-7	32	-22	27	-32	15	-16	-11
Z^m_{xx}(O$_{T1}$)	5	5	6	6	12	16	14	11	0	0
Z^m_{zx}(O$_{T1}$)	191	221	150	154	162	178	150	122	128	105
Z^m_{yy}(O$_{T1}$)	24	23	22	22	31	33	34	25	15	11
Z^m_{xx}(O$_{T2}$)	20	23	16	19	19	22	17	12	25	20
Z^m_{zx}(O$_{T2}$)	195	217	140	161	173	189	166	134	130	110
Z^m_{yy}(O$_{T2}$)	-59	-61	-48	-46	-57	-60	-57	-45	-41	-42
Z^m_{xx}(O$_{P1}$)	-445	-510	-392	-422	-532	-602	-564	-499	-665	-609
Z^m_{xx}(O$_{P2}$)	241	234	215	202	298	299	316	247	388	356
Z^m_{yx}(O$_{P2}$)	-378	-422	-335	-355	-466	-506	-498	-427	-673	-621

TABLE VII. Computed MECs α_{zz} (longitudinal) and α_{xx} and α_{yx} (transverse) for RMnO$_3$ and LuFeO$_3$ (ps/m). Spin-lattice, spin-electronic, and total spin couplings are given as computed with and without SOC.

	Spin-latt.		Spin-elec.		Total spin	
	Total	No SOC	Total	No SOC	Total	No SOC
α_{zz} in A$_2$ phase						
HoMnO$_3$	-0.27	0	0.06	0	-0.21	0
ErMnO$_3$	-0.26	0	0.05	0	-0.21	0
YbMnO$_3$	-0.25	0	0.06	0	-0.19	0
LuMnO$_3$	-0.19	0	0.00	0	-0.19	0
LuFeO$_3$	0.26	0	0.00	0	0.26	0
α_{xx} in A$_2$ phase						
HoMnO$_3$	-0.99	5.12	4.10	4.83	3.11	9.95
ErMnO$_3$	-1.30	2.40	2.56	3.72	1.26	6.12
YbMnO$_3$	-2.52	1.20	3.72	4.66	1.20	5.86
LuMnO$_3$	-2.60	1.31	3.82	3.50	1.22	4.81
LuFeO$_3$	-2.20	-1.57	-0.79	-0.32	-2.99	-1.89
α_{yx} in A$_1$ phase						
HoMnO$_3$	9.55	4.88	5.24	5.35	14.79	10.23

$\sim$0.25 ps/m. The results are comparable to those reported for the transverse MEC in Cr$_2$O$_3$ [36] and for α_{zz} in ErMnO$_3$ [15] in previous first-principles calculations. In the second part of Table VII, we present the spin-related transverse MECs α_{xx} for RMnO$_3$ and LuFeO$_3$ in the A$_2$ phase. The same information is presented in graphical form in Fig. 3.

It is clear from the comparison between the first and second parts of Table VII that the transverse spin-lattice MECs are one order of magnitude larger than the longitudinal ones due to the exchange-striction mechanism. Surprisingly, Fig. 3(a) shows that the effect of SOC on the exchange striction is profound, even reversing the sign of the spin-lattice MECs in RMnO$_3$. This unusual behavior can be traced mainly to two observations about the spin-lattice contributions from different IR-active modes in the RMnO$_3$ materials. Firstly, the exchange-striction MEC is smaller than expected as a result of a large degree of cancellation between the contributions from different transverse IR-active modes. To illustrate this, the mode-by-mode contributions are presented for a few selected cases in Table VIII. Secondly, the softest modes are dominated by Mn displacements, precisely those for which SOC has the largest effect on the Z^m values, even flipping the sign of some components. In this way, it turns out that SOC can result in large relative changes in the MEC results. In the case of LuFeO$_3$, the SOC effect on the Z^m values is weak, even for Fe atoms. Thus, the MEC of LuFeO$_3$ does not change as dramatically as that of RMnO$_3$ when SOC is included.

From Fig. 3(b) it can be seen that the spin-electronic contribution is not negligible in the transverse direction, and it counteracts the MEC from the spin-lattice channel in A$_2$ phase RMnO$_3$. The total transverse ME effect is summarized in Fig. 3(c). Because of the large SOC effect and the cancellation between the lattice and electronic contributions, the total spin MEC α_{xx} is $\sim$1.2 ps/m in most A$_2$-phase RMnO$_3$ compounds, except for HoMnO$_3$. In HoMnO$_3$, the cancellation between the spin-lattice and the spin-electronic MECs is the weakest of all
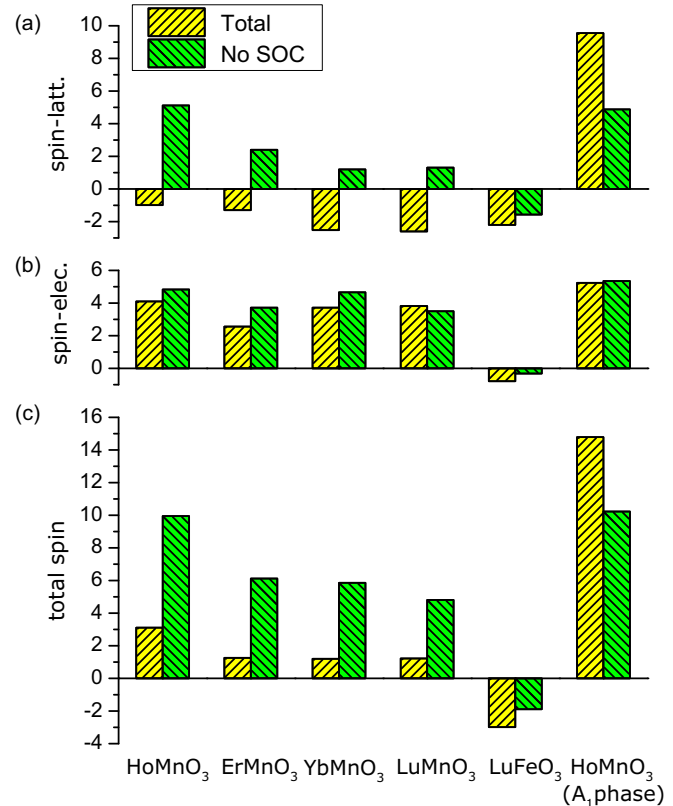

FIG. 3. (Color online) Transverse MECs for RMnO$_3$ and LuFeO$_3$. α_{xx} (ps/m) in the A$_2$ phase and α_{yx} in the A$_1$ phase. (a) Spin-lattice, (b) spin-electronic, and (c) total spin couplings.

the RMnO$_3$ compounds, resulting in the largest total spin MEC of $\sim$3.1 ps/m in the A$_2$ phase. In LuFeO$_3$, the spin-lattice and spin-electronic terms are all smaller than in RMnO$_3$. However,

TABLE VIII. Transverse MEC contributions (ps/m) from IR-active modes for A$_2$ and A$_1$ phases of HoMnO$_3$ and A$_2$ phase of LuMnO$_3$. Results are given in ascending order of force-constant eigenvalues, which are reported in Table II of the Supplemental Material (Ref. [35]).

A$_2$ phase HoMnO$_3$		A$_1$ phase HoMnO$_3$		A$_2$ phase LuFeO$_3$	
Total	No SOC	Total	No SOC	Total	No SOC
0.01	0.12	0.25	0.18	0.28	0.39
-1.16	2.62	4.98	2.36	-0.54	-0.50
0.66	2.32	3.59	2.37	-1.31	-1.22
-0.51	-0.35	-0.32	-0.48	1.30	1.23
2.79	3.13	2.87	3.33	3.31	3.12
0.35	0.21	0.30	0.30	1.84	1.73
-1.88	-1.85	-1.35	-1.90	-4.43	-4.11
1.13	1.25	1.19	1.38	-2.59	-2.25
-2.96	-3.07	-2.70	-3.40	1.24	1.13
0.01	0.13	0.19	0.06	-1.48	-1.27
0.21	0.24	0.21	0.26	-0.15	-0.14
0.36	0.40	0.34	0.42	0.89	0.83
-0.03	-0.03	-0.03	-0.04	-0.62	-0.55
0.02	0.01	0.03	0.03	0.07	0.03

the cancellation induced by the SOC perturbation and the spin-electronic contribution is avoided, so that LuFeO$_3$ has a large total spin MEC of ~ -3 ps/m.

We present the MECs for HoMnO$_3$ in the A$_1$ phase in the last line of Table VII and in Fig. 3. In principle the MECs of HoMnO$_3$ in the A$_1$ and A$_2$ phases should be the same without SOC, as the two phases only differ by a global spin rotation. This is approximately confirmed by a comparison of the corresponding entries for HoMnO$_3$ in Table VII. The ME contribution from exchange striction (i.e., without SOC) is $\sim$5 ps/m for both the A$_2$ and A$_1$ phases. However, when the effect of SOC is included, the spin-lattice contribution is strongly enhanced by another $\sim$5 ps/m. Furthermore, the spin-electronic MEC has the same sign as the spin-lattice one, which adds $\sim$5 ps/m to the MEC. Therefore, the total spin MEC α_{yx} reaches $\sim$15 ps/m and is the largest in all of the RMnO$_3$ and LuMnO$_3$ materials we studied.

IV. SUMMARY

In summary, we have studied the spin-related magnetic charges and MECs for HoMnO$_3$, ErMnO$_3$, YbMnO$_3$, LuMnO$_3$, and LuFeO$_3$ using first-principles calculations. We confirm that the exchange striction acting on noncollinear spins induces much larger magnetic charges than does SOC acting alone. Nevertheless, the effect of SOC on the MECs is surprisingly large, rivaling that of exchange striction in many cases. This occurs because the exchange-striction contribution tends to be reduced by cancellations between different IR-active modes, while the SOC contribution is mainly associated with just a few low-frequency modes with large Mn displacements. We also find that the RMnO$_3$ materials have spin-electronic MECs comparable to the spin-lattice ones. Among the RMnO$_3$ and LuFeO$_3$ materials we studied, we find that the A$_1$ phase of HoMnO$_3$ is the most promising ME material, with the largest MEC of $\sim$15 ps/m. Extrapolating our conclusions to other hexagonal RMnO$_3$ and RFeO$_3$ compounds that are not included in our calculations, we predict that the A$_2$ phase is more promising for the ferrites, while the A$_1$ phase has a stronger MEC for the manganites.

[1] M. Fiebig, J. Phys. D **38**, R123 (2005).
[2] N. A. Spaldin and M. Fiebig, Science **309**, 391 (2005).
[3] W. Eerenstein, N. D. Mathur, and J. F. Scott, Nature (London) **442**, 759 (2006).
[4] Y. Tokura, J. Magn. Magn. Mater. **310**, 1145 (2007).
[5] S.-W. Cheong and M. Mostovoy, Nat. Mater. **6**, 13 (2007).
[6] R. Ramesh and N. A. Spaldin, Nat. Mater. **6**, 21 (2007).
[7] K. F. Wang, J.-M. Liu, and Z. F. Ren, Adv. Phys. **58**, 321 (2009).
[8] M. Fiebig and N. A. Spaldin, Eur. Phys. J. B **71**, 293 (2009).
[9] J.-P. Rivera, Eur. Phys. J. B **71**, 299 (2009).
[10] D. Khomskii, Physics **2**, 20 (2009).
[11] T. Birol, N. A. Benedek, H. Das, A. L. Wysocki, A. T. Mulder, B. M. Abbett, E. H. Smith, S. Ghosh, and C. J. Fennie, Curr. Opin. Solid State Mater. Sci. **16**, 227 (2012).
[12] E. Bousquet, N. A. Spaldin, and K. T. Delaney, Phys. Rev. Lett. **106**, 107202 (2011).
[13] J. Íñiguez, Phys. Rev. Lett. **101**, 117201 (2008).
[14] K. T. Delaney, M. Mostovoy, and N. A. Spaldin, Phys. Rev. Lett **102**, 157203 (2009).
[15] H. Das, A. L. Wysocki, Y. Geng, W. Wu, and C. J. Fennie, Nat. Commun. **5**, 2998 (2014).
[16] M. Ye and D. Vanderbilt, Phys. Rev. B **89**, 064301 (2014).
[17] M. Mostovoy, Nat. Mater. **9**, 188 (2010).
[18] B. B. Van Aken, T. T. M. Palstra, A. Filippetti, and N. A. Spaldin, Nat. Mater. **3**, 164 (2004).
[19] C. J. Fennie and K. M. Rabe, Phys. Rev. B **72**, 100103 (2005).
[20] Y. Kumagai and N. A. Spaldin, Nat. Commun. **4**, 1540 (2013).
[21] S. Artyukhin, K. T. Delaney, N. A. Spaldin, and M. Mostovoy, Nat. Mater. **13**, 42 (2013).
[22] T. Choi, Y. Horibe, H. T. Yi, Y. J. Choi, W. Wu, and S.-W. Cheong, Nat. Mater. **9**, 253 (2010).

[23] S.-Z. Lin, X. Wang, Y. Kamiya, G.-W. Chern, F. Fan, D. Fan, B. Casas, Y. Liu, V. Kiryukhin, W. H. Zurek, C. D. Batista, and S.-W. Cheong, Nat. Phys. **10**, 970 (2014).
[24] M. Fiebig, Th. Lottermoser, and R. V. Pisarev, J. Appl. Phys. **93**, 8194 (2003).
[25] F. Yen, C. D. Cruz, B. Lorenz, E. Galstyan, and Y. Y. Sun, J. Mater. Res. **22**, 2163 (2007).
[26] B. Lorenz, ISRN Condens. Matter Phys. **2013**, 1 (2013).
[27] Y. Geng, H. Das, A. L. Wysocki, X. Wang, S.-W. Cheong, M. Mostovoy, C. J. Fennie, and W. Wu, Nat. Mater. **13**, 163 (2014).
[28] W. Wang, J. Zhao, W. Wang, Z. Gai, N. Balke, M. Chi, H. N. Lee, W. Tian, L. Zhu, X. Cheng, D. J. Keavney, J. Yi, T. Z. Ward, P. C. Snijders, H. M. Christen, W. Wu, J. Shen, and X. Xu, Phys. Rev. Lett. **110**, 237601 (2013).
[29] S. M. Disseler, J. A. Borchers, C. M. Brooks, J. A. Mundy, J. A. Moyer, D. A. Hillsberry, E. L. Thies, D. A. Tenne, J. Heron, J. D. Clarkson, G. M. Stiehl, P. Schiffer, D. A. Muller, D. G. Schlom, and W. D. Ratcliff, Phys. Rev. Lett. **114**, 217602 (2015).
[30] G. Kresse and J. Furthmüller, Phys. Rev. B **54**, 11169 (1996).
[31] J. P. Perdew, K. Burke, and M. Ernzerhof, Phys. Rev. Lett. **77**, 3865 (1996).
[32] P. E. Blochl, Phys. Rev. B **50**, 17953 (1994); G. Kresse and D. Joubert, *ibid.* **59**, 1758 (1999).
[33] A. I. Liechtenstein, V. I. Anisimov, and J. Zaanen, Phys. Rev. B **52**, R5467 (1995)
[34] R. D. King-Smith and D. Vanderbilt, Phys. Rev. B **47**, 1651 (1993).
[35] See Supplemental Material at http://link.aps.org/supplemental/ 10.1103/PhysRevB.92.035107 for information of the Born charge tensors and the force-constant eigenvalues for the other material covered by this study.
[36] A. Malashevich, S. Coh, I. Souza, and D. Vanderbilt, Phys. Rev. B **86**, 094430 (2012).